Korean J. Chem. Eng., 40(4), 754-769 (2023)
DOI: 10.1007/s11814-022-1343-5

pISSN: 0256-1115
eISSN: 1975-7220

An investigation on the effect of open hole number and scheme on single-phase flow of a swirl flow bubble generator

Yuxue Wu*,, Hang Chen*,**,†, and Xingfu Song*,**,†**

*National Engineering Research Center for Integrated Utilization of Salt Lake Resource, East China University of Science and Technology, Shanghai 200237, China
**Joint International Laboratory for Potassium and Lithium Strategic Resources, East China University of Science and Technology, Shanghai 200237, China
(*Received 1 March 2022 • Revised 14 September 2022 • Accepted 6 November 2022*)

Abstract−A swirl flow bubble generator with a unique adjustment scheme was developed to adapt to liquid feed flow rate variation. However, a study on the scheme and flow field of the bubble generator has not been reported in the literature. Particle image velocimetry and computational fluid dynamics were utilized to explore the flow field and adjustment scheme. The results showed that the standard k-ε model could more accurately describe the flow pattern than other turbulence models, and the pressure drop difference between experiments and simulations was less than 6%. A mathematical expression was established to quantitatively describe the relationship among the pressure drop, open hole number, and liquid flow rate. The pressure drop was proportional to the feed flow rate or inlet velocity square and inversely proportional to the power of 1.86 of the open hole number. Interestingly, the pressure drop of different open hole schemes with the same open hole number of 12 was close to 55 kPa. The spiral-bottom open hole schemes could provide a higher turbulent dissipation rate for both the vortex chamber and straight pipe section. This work can guide the bubble generator adjustment and fill the gap in this respect.

Keywords: Computational Fluid Dynamics (CFD), Open Hole Number, Open Hole Scheme, Swirl Flow Bubble Generator

INTRODUCTION

Flotation as a secondary treatment technology in oily wastewater has been widely applied [1-3]. One of the most critical components in the flotation system is the bubble generator because the bubble size and concentration are directly related to the collision, attachment, and detachment between the bubbles and oil droplets [4]. Hence, some investigations on the bubble generator should be paid more attention. Recently, various bubble generators have been reported, such as venturi type [5], pressurized dissolution type [6], membrane type [7], and swirl flow type [8]. Due to the high turbulence environment, the swirl flow bubble generator has more advantages in the bubble generation performance.

The swirl flow bubble generator has been proven to have a significant advantage in bubble generation and oxygen dissolution performance. Terasaka et al. [9] compared several kinds of bubble generators to explore the oxygen dissolution performance in water. The results indicate that the oxygen transfer coefficient in the swirl flow bubble generator is higher than other bubble generators at a low superficial gas velocity of less than 0.001 m/s. Kim et al. [10] utilized the swirl flow bubble generator to intensify the membrane flux in a multistage direct contact membrane distillation system. Indeed, the mean transmembrane flux is enhanced by ~26% to the maximum extent assisted with the swirl flow bubble generator at a feed temperature of 40 °C and feed flow rate of 120 L/h. Wang et al. [11] added four tangential inlets in the traditional venturi type bubble generator to introduce a swirl flow pattern. Due to the higher turbulent dissipation provided by swirl flow, the swirl-venturi bubble generator reduces the Sauter mean diameter by 48.3% at the superficial liquid velocity of 0.32 m/s and superficial gas velocity of 0.013 m/s. Wu et al. [12] modified the conventional venturi tube using the fan-shaped baffle inlet and spiral channel in the converging section. The optimized swirl-venturi bubble generator installed downstream of the venturi tube formed a micro-nano bubble generator, which can generate bubbles with a mean diameter of 1.74 μm, two orders of magnitude smaller than the traditional venturi tube. Moreover, the dissolved oxygen is enhanced by 36.06%.

In the last ten years, more and more scholars have focused on the swirl flow bubble generator. Levitsky et al. [13] designed a bubble generator with a vortex chamber radius of 5.2 mm. At the liquid flow rate of 60 L/h, the number of bubbles with diameters less than 20 μm is more than 90%. Xu et al. [14] explored the effect of nozzle diameter on the bubble size distribution and spray morphology in a swirl flow bubble generator. When the nozzle diameter exceeds 8.6 mm, the generator begins to achieve gas self-suction. There is a minimum mean bubble size of 0.27 mm at the nozzle diameter of 21.6 mm with a pump pressure of 0.1 MPa. Mawarni et al. [15] developed a swirl flow bubble generator and studied the effect of two-phase flow rates and the gap between the air nozzle and the generator outlet on the performance of the swirl flow bubble generator. Increasing the gas flow rate leads to increasing the mean bubble size and reducing the oxygen mass transfer coeffi-

†To whom correspondence should be addressed.
E-mail: chenhang@ecust.edu.cn, xfsong@ecust.edu.cn
Copyright by The Korean Institute of Chemical Engineers.

cient, while for the increase in the liquid flow rate, the opposite results are obtained. The gap of 1 mm has a smaller and more uniform bubble size than other distances. Chang et al. [16] utilized a gas-liquid swirling-sparger to generate a mean bubble diameter of 0.625 mm, and the oxygen absorption efficiency is more than 70% at an inlet flow rate of 1.3 m^3/h. In general, the investigation on the swirl flow bubble generator is greatly meaningful.

In 2003-2004, the University of Utah and the Clean Water Technology (CWT) [17] company invented a second-generation flotation device, which directly uses influent wastewater to generate bubbles. Due to many oblique holes, the bubble generator can be considered a swirl flow type. The unique structure makes the bubble generator have a different running mode. As the feed flow rate changes considerably, the oblique holes can be opened or closed to fit the flow rate variation to ensure the mixing energy in the bubble generator. However, the adjustment mode usually depends on the experience without guidance on the theoretical level, and the unique adjustment technology has not been reported in the present literature for the bubble generator. At present, various experiment technologies have been developed to detect the bubbles or cavitation and measure the flow field, such as vibration and spectrum analysis [18-21], acoustic analysis [22-24], high-speed camera [7,12,15], and particle image velocimetry (PIV) [25-28]. Meanwhile, with the development of computer hardware and mathematical models, using computational fluid dynamics (CFD) for studying chemical mechanical devices has become increasingly common. Al-Obaidi et al. [29-36] successfully involved CFD numerical simulations in the pump unit operation. The simulation studies on the bubble generator are also in some literature [16,37]. It indicates that the CFD technique is promising for exploring device performance from the flow field aspect and reducing the experiment cost.

In this paper, single-phase flow of a swirl flow bubble generator was studied using the PIV and CFD techniques. The aim of the work was to study the effect of open hole number and open hole scheme on the flow field and provide guidance from the theoretical level for the special adjustment mode. Firstly, the local flow field information of the device was obtained through PIV experiments, which were used to validate and select suitable turbulence models. Then, single-phase flow field analysis was carried out in terms of the pressure, velocity, and turbulence characteristics. Next, the relationship among the pressure drop, open hole number, and liquid feed flow rate was established quantificationally. Finally, the differences of some general open hole schemes were compared. This work can provide a clear guideline on the special adjustment mode.

EXPERIMENTS AND METHODS

1. Geometry

A CAD drawing of the swirl flow bubble generator is shown in Fig. 1(a). It mainly consists of the annular cavity, vortex chamber, and straight pipe section. The influent wastewater enters the annular cavity 10 from the liquid inlet 9 and injects into the vortex chamber 8 along the multiple oblique holes 6 in the inner cylinder wall 7. The function of the cavity can make the liquid evenly flow into the vortex chamber, improving the stability of the flow field. The core component is the inner cylinder wall with oblique holes whose purpose is to generate a swirl flow field in the vortex chamber and straight pipe section. In the inner cylinder wall, there are 72 holes connecting the annular cavity and vortex chamber. These holes are divided into 6 columns uniformly along the circumference and 12

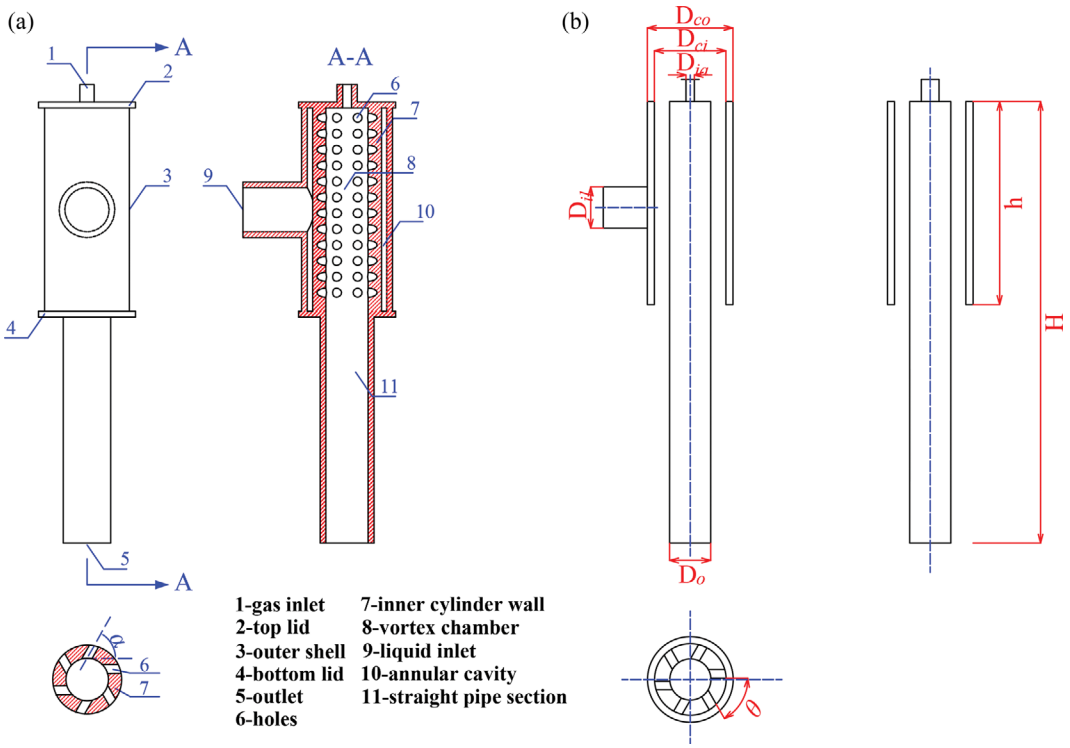


Fig. 1. (a) CAD drawing and (b) three views of the swirl flow bubble generator.

Table 1. Partial structural dimensions of the swirl flow bubble generator

Symbol	Value (m)	Symbol	Value (m)
D_o	0.044	D_{co}	0.097
D_{ci}	0.081	D_{il}	0.041
d	0.003	D_{ia}	0.020
H	1.500	h	0.230

holes uniformly distribute at each column along the height direction. The hole central axis horizontal angle α is 60°. These oblique holes can be opened or closed to respond to the variation of the liquid feed flow rate. When the feed flow rate reduces significantly, plugging holes can ensure a high turbulent intensity in the vortex chamber. The calculated fluid domain was extracted from the 3D CAD drawing using the ANSYS SCDM software, as shown in Fig. 1(b). The angle between the central axes of adjacent holes on the circumference is 60°. In the height direction, the vertical distance of adjacent holes is 17.36 mm. Table 1 lists the other geometry sizes of the swirl flow bubble generator.

2. Experiments

A schematic diagram of the experimental device is shown in Fig. 2(a). It mainly contained a centrifugal pump (ISW50-200I), an electromagnetic flow meter (DJLD-4032), a swirl flow bubble generator, and a recycle water tank (304 stainless steel, V=400 L) to form a circulation loop. The PIV measurements were only carried out on the single-phase flow. Considering the observation of the vortex chamber affected by the inner cylinder wall and the complex flow, it is challenging for us to directly measure the flow field of the vortex chamber. Therefore, the actual measurement location was located at the straight pipe section. The measurement position has been labeled in Fig. 2(a), and the window size was 44 mm× 60 mm. The selected region was close to the vortex chamber and away from the outlet. On the one hand, it can quickly respond to the flow field variation of the vortex chamber. On the other hand, the outlet reverse flow cannot affect the region flow significantly. Before starting the PIV measurement, reduce the globe valve 11 opening and open the vent valve 8 to remove the air from the generator 9. Once the air has been exhausted, close the vent valve 8 and open the globe valve 11 fully to begin the experiments.

Fig. 2(b) shows a schematic diagram of the PIV system. The PIV measurements were carried out using a double-pulse laser with a wavelength of 532 nm and a pulse frequency of 10 Hz (Continuum Inc., USA). The laser beam passed through an optical device consisting of a cylindrical and spherical lens to produce laser sheets of approximately 2 mm thickness. The images were obtained by a high-speed charge coupled device (CCD) camera (PowerView Plus, TSI, USA) with a resolution of 2,048×2,048 pixels. The camera and laser were controlled by a laser pulse 610035 synchronizer (TSI, USA). A cube Plexiglas box was filled with water before the test to minimize light refraction on the curved surface of the tube. In this work, a non-fluorescent hollow glass sphere with a diameter of 100 μm was selected as the tracer particle because the size could be captured clearly. During the measurements, the time interval between the two frames was 50 μs to identify the particle displacement in the two frames. The obtained images were processed by Insight 4G software using the velocity cross-correlation analysis algorithm. The CCD camera captured 200 image pairs in each experiment. Finally, the average velocity of 200 image pairs was processed using Tecplot software.

Apart from the PIV measurement, pressure drop measurements were also conducted. The pressure drop is defined as the pressure difference between the liquid inlet and outlet, namely, $\Delta P=P_{in}-P_{out}$. In this work, the pressures of the inlet and outlet were measured by the pressure gauge (MEACON, SUP-Y810, 0-0.6 MPa, ±0.5%).

NUMERICAL SIMULATIONS

1. Turbulence Models

Reynolds-Averaged Navier-Stokes (RANS) turbulence models were used to describe the turbulence environment in the swirl flow bubble generator because of their high accuracy and low calculation cost. The RANS equations expressed by the Cartesian tensor form are listed as follows. There are additional terms $-\rho\overline{u_i'u_j'}$ appearing on the right side of Eq. (2). Therefore, it must be modeled by introducing new turbulence models to close the equations:

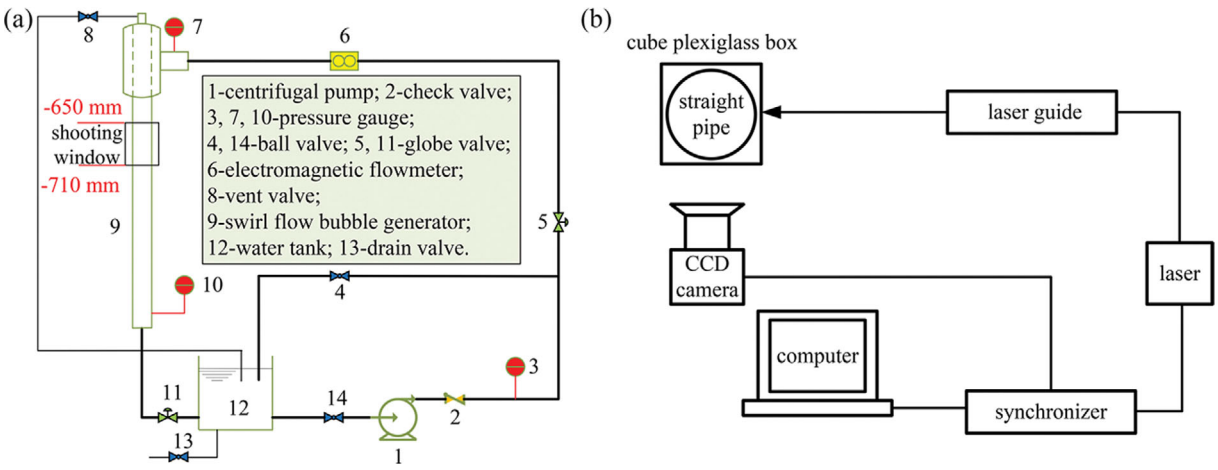


Fig. 2. (a) The schematic diagram of the experimental system, and (b) PIV test system.

$$\frac{\partial \rho}{\partial t}+\frac{\partial}{\partial x_i}(\rho u_i)=0 \tag{1}$$

$$\frac{\partial(\rho u_i)}{\partial t}+\frac{\partial(\rho u_i u_j)}{\partial x_j}=-\frac{\partial p}{\partial x_i}+\frac{\partial}{\partial x_j}\left(\mu\frac{\partial u_i}{\partial x_j}-\rho\overline{u_i' u_j'}\right) \tag{2}$$

where ρ is the fluid density. u and p denote the fluid velocity and pressure, respectively. μ is the fluid viscosity. The subscripts i and j represent the tensor form.

To select suitable turbulence models, the standard k-ε model [38], renormalization group (RNG) k-ε model [39], realizable k-ε model [40], shear stress transport (SST) k-ω model [41], and Reynolds stress model (RSM) [42-44] for the incompressible fluid were compared. The equations of these turbulence models are listed as follows.

1-1. Standard k-ε Model

The standard k-ε model is based on the transport equations of turbulent kinetic energy k and dissipation rate ε, which is one of the broadest application turbulence models at present.

$$\frac{\partial(\rho k)}{\partial t}+\frac{\partial(\rho k u_i)}{\partial x_i}=\frac{\partial}{\partial x_j}\left[\left(\mu+\frac{\mu_t}{\sigma_k}\right)\frac{\partial k}{\partial x_j}\right]+G_k-\rho\varepsilon \tag{3}$$

$$\frac{\partial(\rho\varepsilon)}{\partial t}+\frac{\partial(\rho\varepsilon u_i)}{\partial x_i}=\frac{\partial}{\partial x_j}\left[\left(\mu+\frac{\mu_t}{\sigma_\varepsilon}\right)\frac{\partial \varepsilon}{\partial x_j}\right]+C_{1\varepsilon}\frac{\varepsilon}{k}G_k-C_{2\varepsilon}\rho\frac{\varepsilon^2}{k} \tag{4}$$

$$\mu_t=\rho C_\mu\frac{k^2}{\varepsilon},\ G_k=\mu_t\left(\frac{\partial u_i}{\partial x_j}+\frac{\partial u_j}{\partial x_i}\right)\frac{\partial u_i}{\partial x_j} \tag{5}$$

$$C_{1\varepsilon}=1.44,\ C_{2\varepsilon}=1.92,\ C_\mu=0.99,\ \sigma_k=1.0,\ \sigma_\varepsilon=1.3 \tag{6}$$

where μ_t denotes the turbulent viscosity. G_k is the generation term of k resulting from the mean velocity gradient. $C_{1\varepsilon}$ and $C_{2\varepsilon}$ are empirical constants, respectively. σ_k and σ_ε are the Prandtl numbers for k and ε, respectively.

1-2. RNG k-ε Model

By correcting the turbulent viscosity, the RNG k-ε model considers the rotation and swirl flow and adds a term to the ε equation to reflect the time-averaged strain rate E_{ij}.

$$\frac{\partial(\rho k)}{\partial t}+\frac{\partial(\rho k u_i)}{\partial x_i}=\frac{\partial}{\partial x_j}\left[\alpha_k(\mu+\mu_t)\frac{\partial k}{\partial x_j}\right]+G_k-\rho\varepsilon \tag{7}$$

$$\frac{\partial(\rho\varepsilon)}{\partial t}+\frac{\partial(\rho\varepsilon u_i)}{\partial x_i}=\frac{\partial}{\partial x_j}\left[\alpha_\varepsilon(\mu+\mu_t)\frac{\partial \varepsilon}{\partial x_j}\right]+C_{1\varepsilon}^*\frac{\varepsilon}{k}G_k-C_{2\varepsilon}\rho\frac{\varepsilon^2}{k} \tag{8}$$

$$C_{1\varepsilon}^*=C_{1\varepsilon}-\frac{\eta(1-\eta/\eta_0)}{1+\beta\eta^3},\ \eta=E\frac{k}{\varepsilon},\ E=(2E_{ij}\cdot E_{ij})^{1/2},$$

$$E_{ij}=\frac{1}{2}\left(\frac{\partial u_j}{\partial x_i}+\frac{\partial u_i}{\partial x_j}\right) \tag{9}$$

$$C_{1\varepsilon}=1.42,\ C_{2\varepsilon}=1.68,\ C_\mu=0.0845,\ \alpha_k=\alpha_\varepsilon=1.39,$$
$$\eta_0=4.377,\ \beta=0.012 \tag{10}$$

1-3. Realizable k-ε Model

The Realizable k-ε model also considers the effect of rotation and curvature by modifying the turbulent viscosity. It has been widely applied in swirl shear, jet, and boundary layer flow.

$$\frac{\partial(\rho k)}{\partial t}+\frac{\partial(\rho k u_i)}{\partial x_i}=\frac{\partial}{\partial x_j}\left[\left(\mu+\frac{\mu_t}{\sigma_k}\right)\frac{\partial k}{\partial x_j}\right]+G_k-\rho\varepsilon \tag{11}$$

$$\frac{\partial(\rho\varepsilon)}{\partial t}+\frac{\partial(\rho\varepsilon u_i)}{\partial x_i}=\frac{\partial}{\partial x_j}\left[\left(\mu+\frac{\mu_t}{\sigma_\varepsilon}\right)\frac{\partial \varepsilon}{\partial x_j}\right]+\rho C_1 E\varepsilon-\rho C_2\frac{\varepsilon^2}{k+\sqrt{v\varepsilon}} \tag{12}$$

$$C_1=\max\left(0.43,\ \frac{\eta}{\eta+0.5}\right) \tag{13}$$

$$C_\mu=\frac{1}{4.04+\sqrt{6}\cos\phi U^* k/\varepsilon},\ \phi=\frac{1}{3}\cos(\sqrt{6}W),\ W=\frac{E_{ij}E_{jk}E_{kj}}{(E_{ij}E_{ij})^{1/2}}, \tag{14}$$

$$U^*=\sqrt{E_{ij}E_{ij}+\tilde{\Omega}_{ij}\tilde{\Omega}_{ij}},\ \tilde{\Omega}_{ij}=\Omega_{ij}-2\varepsilon_{ijk}\omega_k,\ \Omega_{ij}=\tilde{\Omega}_{ij}-\varepsilon_{ijk}\omega_k$$
$$\sigma_k=1.0,\ \sigma_\varepsilon=1.2,\ C_2=1.9 \tag{15}$$

where $\tilde{\Omega}_{ij}$ is the mean rate-of-rotation tensor viewed in a moving reference frame with the angular velocity ω_k.

1-4. SST k-ω Model

The SST k-ω model is an improvement on the standard k-ω model. In addition, turbulent shear stress transport is considered in the turbulent viscosity. Therefore, the SST k-ω model is more accurate and reliable in various types of flows, for example, adverse pressure gradient flow, than the standard k-ω model:

$$\frac{\partial(\rho k)}{\partial t}+\frac{\partial(\rho k u_i)}{\partial x_i}=\frac{\partial}{\partial x_j}\left[\left(\mu+\frac{\mu_t}{\sigma_k}\right)\frac{\partial k}{\partial x_j}\right]+G_k-Y_k \tag{16}$$

$$\frac{\partial(\rho\omega)}{\partial t}+\frac{\partial(\rho\omega u_i)}{\partial x_i}=\frac{\partial}{\partial x_j}\left[\left(\mu+\frac{\mu_t}{\sigma_\omega}\right)\frac{\partial \omega}{\partial x_j}\right]+G_\omega-Y_\omega \tag{17}$$

$$\mu_t=\frac{\rho k}{\omega}\frac{1}{\max\left[\frac{1}{\alpha^*},\ \frac{SF_2}{\alpha_1\omega}\right]},\ F_2=\tanh(\Phi_2^2),$$

$$\Phi_2=\max\left(\frac{2\sqrt{k}}{0.09\omega y},\ \frac{500\mu}{\rho y^2\omega}\right) \tag{18}$$

$$\sigma_k=\sigma_\omega=2.0 \tag{19}$$

where G_ω is the generation of ω. Y_k and Y_ω denote the dissipation of k and ω due to turbulence. S is the magnitude of the strain force. y represents the distance to the next surface.

1-5. RSM

The anisotropic problem is considered in RSM. Compared to two-equation models, RSM considers more strictly the effects of streamline curvature, eddy, rotation, and rapid changes in strain rate. Therefore, it has more potential to predict complex flows accurately. Different from the other turbulence models, RSM directly divides the Reynolds stress term $-\rho\overline{u_i' u_j'}$ into five terms, namely:

$$\frac{\partial(\rho\overline{u_i' u_j'})}{\partial t}+\frac{\partial(\rho u_k\overline{u_i' u_j'})}{\partial x_k}=D_{T_{ij}}+P_{ij}+\phi_{ij}+\varepsilon_{ij}+F_{ij} \tag{20}$$

Turbulent diffusion term:

$$D_{T_{ij}}=-\frac{\partial}{\partial x_k}[\rho\overline{u_i' u_j' u_k'}+\overline{p'(\delta_{kj}u_i'+\delta_{ik}u_j')}] \tag{21}$$

Stress production term:

$$P_{ij}=-\rho\left(\overline{u_i' u_k'}\frac{\partial u_j}{\partial x_k}+\overline{u_j' u_k'}\frac{\partial u_i}{\partial x_k}\right) \tag{22}$$

Pressure strain term:

$$\phi_{ij}=p'\left(\frac{\partial u_i'}{\partial x_j}+\frac{\partial u_j'}{\partial x_i}\right) \tag{23}$$

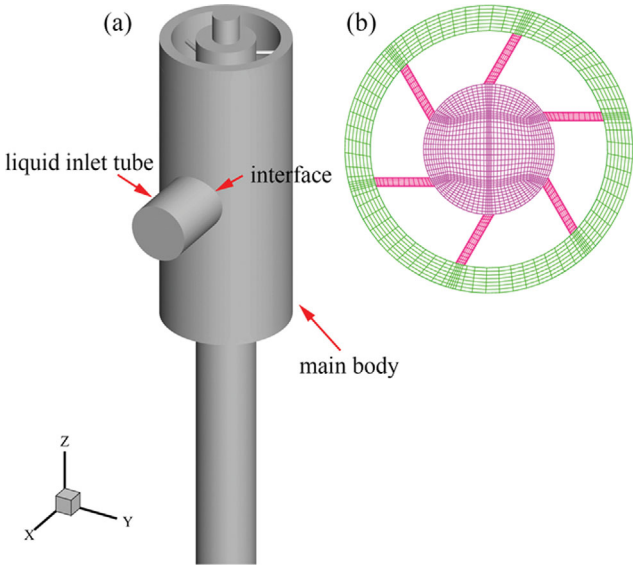


Fig. 3. (a) Geometry and (b) mesh of the swirl flow bubble generator.

Dissipation term:

$$\varepsilon_{ij}=-2\mu\left(\overline{\frac{\partial u_i'}{\partial x_k}}\overline{\frac{\partial u_j'}{\partial x_k}}\right) \tag{24}$$

Production of system rotation term:

$$F_{ij}=-2\rho\Omega_k(\overline{u_j'u_m'}\varepsilon_{ikm}+\overline{u_i'u_m'}\varepsilon_{jkm}) \tag{25}$$

2. Mesh Generation and Independence

First, the ANSYS SCDM software was used to construct the 3D geometry, which was divided into two parts: liquid inlet tube and main body part. Then, the two parts were blocked into hexahedral mesh by ANSYS ICEM CFD software using the default BiGeometric mesh distribution law, as shown in Fig. 3. Finally, the generated mesh was imported into CFD solver FLUENT, and the data communication between the two parts used the interface method. The inflation layer is subject to the wall function in turbulence. Here, the standard wall function was adopted to avoid the fine mesh along the wall, and the Y^+ value was ~30.

To ensure the simulated accuracy and reduce the calculation time, it is necessary to make mesh independence validation. The grids 209940, 418990, 645494, and 744894 were used to test. At a liquid feed flow rate of 5.56E-4 m^3/s, the mean axial velocity and mean turbulent dissipation rate with different mesh scales were compared at the height of Z=−80 mm in the vortex chamber, as shown in Fig. 4. When the number of grids is greater than 418990, the variation of mean axial velocity and mean turbulent dissipation rate can be ignored. Therefore, the grids with 418990 were selected for the subsequent simulations.

3. Boundary Conditions and Simulation Setting

In this paper, only the liquid phase was considered. Its density and viscosity are 998.2 kg/m^3 and 0.001003 Pa·s at room temperature, respectively. The inlet and outlet boundary types were velocity-inlet and pressure-outlet, respectively. The corresponding boundary condition equations are displayed in Eqs. (26) and (27). The specification method of turbulence involves turbulent intensity and hydraulic diameter. The turbulent intensity was set as 5%, and the hydraulic diameter was consistent with the inlet or outlet diameter. The 5% turbulent intensity is suitable for a modest turbulence environment, which is the common setting inlet turbulence condition method. Yan et al. [45] also adopted the "Intensity and Hydraulic Diameter" method to set the initial turbulence conditions at the inlet and outlet in a gas-liquid bubble column. The wall adopted the no-slip boundary condition, and the standard wall function was adopted near the wall.

velocity-inlet

$$u(x)=-u_0,\ u(y)=u(z)=0 \tag{26}$$

pressure-outlet

$$p_{out}=0 \tag{27}$$

where u_0 is the liquid inlet velocity magnitude.

In this study, the pressure-based solver and transient simulations were considered. The pressure-implicit with splitting of operators (PISO) algorithm was adopted for the pressure-velocity coupling scheme. Gradient and pressure were estimated by the least squares cell-based method and pressure staggering option (PRESTO!) scheme, respectively. Moreover, quadratic upstream interpolation for convective kinematics (QUICK) scheme was adopted for the momentum, the turbulent kinetic energy, and the turbulent dissi-

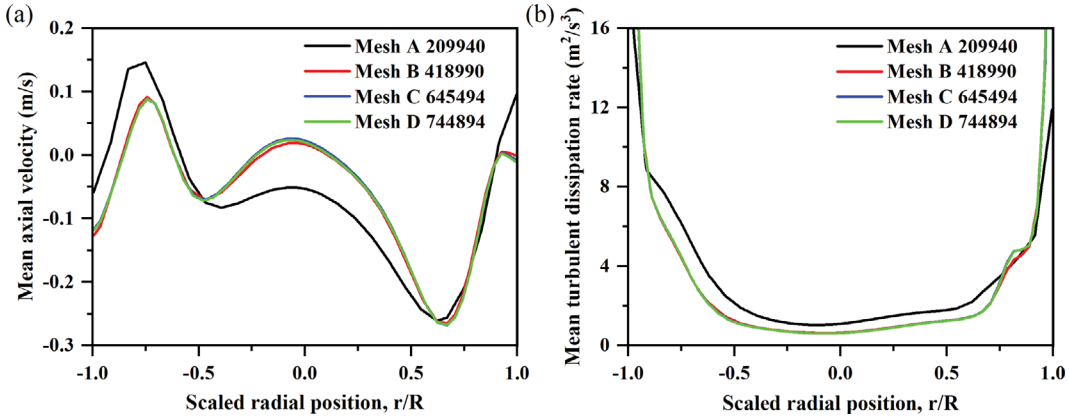


Fig. 4. The mesh independence on (a) mean axial velocity and (b) mean turbulent dissipation rate.

pation rate discretization. The solution was controlled by under-relaxation factors. The under-relaxation factors of pressure and momentum equations were set as 0.3 and 0.7, respectively. Moreover, the under-relaxation factors of both turbulent kinetic energy and turbulent dissipation rate equations were set as 0.8, and others were default values. The time step size was 0.0005 s, and all scaled residuals for the equations convergence criteria were less than 10^{-4}. The max iterations were set as 20. The flow field used the standard initialization method, and the velocity was initialized as inlet velocity, as shown in Eq. (28). When the calculation time was greater

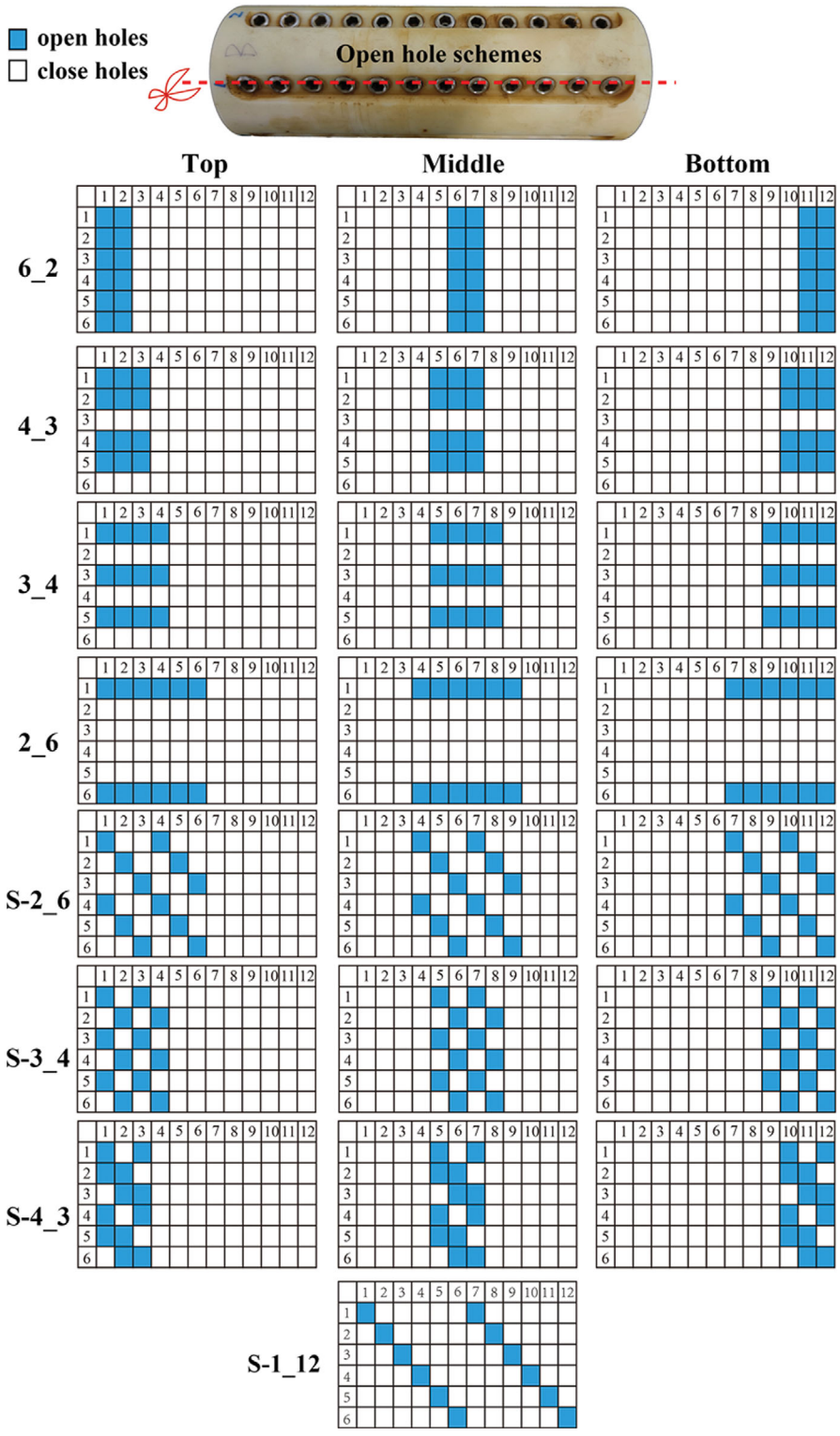


Fig. 5. Several typical open hole schemes.

than 10 s, the monitored velocity magnitude of the outlet was stable, and the calculation was regarded as convergence. Then, we continued calculating for 5 s, and took the average of 5 s data as the final simulation results for all cases.

$$u(x, t=0) = -u_0,\ u(y, t=0) = u(z, t=0) = 0 \quad (28)$$

4. Explanation of the Open Hole Number and Scheme

The open hole number refers to the number of the open holes in the inner cylinder wall. The open hole number is increased or decreased according to the variation of the feed flow rate. The open hole scheme means that when the open hole number and feed flow rate are not changed, there are many schemes for open holes. As an example of open hole number of 12, there are a total of C_{72}^{12} open hole schemes. It is impossible to compare the differences of all the open hole schemes. Therefore, several typical open hole schemes were selected here, such as the top, middle, bottom, and spiral open hole schemes, as shown in Fig. 5. A blue box means that the hole is open, and a white box indicates that it is closed. S represents the spiral open hole schemes. The open hole number and scheme adjustments were achieved by applying wall boundaries inside the holes during the simulations.

RESULTS AND DISCUSSION

1. PIV Measurement Results and Models Validation

At the liquid flow rate of 5.56E-4 m^3/s, the open hole number of 12, and the open hole scheme S-1_12, the results predicted by the above-mentioned turbulence models were compared with the PIV experimental data, as shown in Fig. 6. It shows the mean axial velocity of the swirl flow bubble generator at Z=−680 mm. The short error bars indicate the accuracy of the measurement results. The values predicted by the standard k-ε were closest to the experimental values, and the errors of other turbulence models were relatively large. Alam et al. [8] also validated the reliability of the standard k-ε in a swirl flow bubble generator. Although the standard k-ε model had the best compatibility among these turbulence models, there were still some differences compared with the PIV results, especially in the central region with the simulation of the velocity profile deviating from the experimental data by a factor of 2. The reasons can be explained as follows: (1) the actual geometry, especially the inner cylinder, has various tiny configurations such as guide groove and internal thread in open hole inner face. However, these structures were ignored during simulations to simplify the modeling process. A pipe with a diameter of 3 mm replaced the actual holes. (2) The errors can be from the PIV shooting process, such as the shooting plane of nonuniform illumination and the image noise with bad points. (3) The density of tracer particles with a diameter of 100 μm is less than the density of water. Due to swirl flow, the particles can aggregate at the center of the pipe, leading to significant errors in the central region. Therefore, it is not easy to achieve complete consistency. Although RSM is the most robust RANS based turbulence model, it produced the maximum deviation in comparison with the PIV data in this paper. It is possible that RSM mainly applies in the strong swirl and shear flows, overestimating the swirl flow pattern in the swirl flow bubble generator. Hence, the selection of the turbulence model should be based on the experimental data.

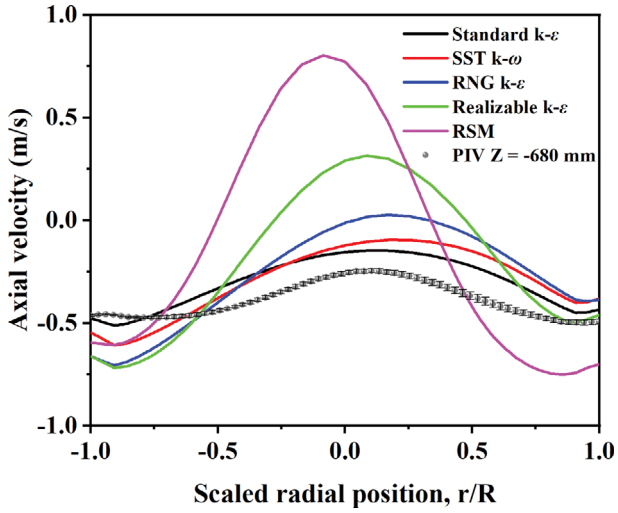


Fig. 6. Comparison of axial velocity between turbulence models and PIV experiments at Z=−680 mm.

Fig. 7(a) shows the two frames A and B image analysis results using Insight 4G software. The final velocity vectors were averaged by Tecplot software, as shown in Fig. 7(b). It was found that velocity vectors were along the downward right direction without the upward arrows. It indicated curvature flow in the straight pipe section, but the swirl flow was not strong enough to produce the eddy. In the radial direction, the velocity magnitude increased and then decreased. Near position Y=0, the velocity magnitude had the maximum value of ~0.75 m/s. Fig. 7(c) shows the velocity vector calculated by different turbulence models in the X=0 plane. The results of the standard k-ε model were consistent with the PIV. However, other turbulence models overestimated the presence of vortices in the flow field. RNG k-ε, Realizable k-ε, and RSM are primarily applied in the strong turbulent environment, for example, hydrocyclone [46]. Meanwhile, the holes and vortex chamber diameters in the swirl flow bubble generator are 3 mm and 44 mm, respectively. The almost 15 times difference makes the flow field of the device different from that of the hydrocyclone. Here, we chose the standard k-ε model to analyze the flow field further. PIV was only used to obtain the local flow field distribution, and it did not measure the flow in the vortex chamber in this paper. Therefore, it was necessary to use the CFD numerical simulation method to analyze the flow of the entire equipment, which included the vortex chamber and the straight pipe section.

The whole pressure drops of the equipment predicted by the standard k-ε model were compared with the measured values, as shown in Fig. 8. The open hole number was 12, and the open hole scheme was S-1_12. With the increase in the feed flow rate, the pressure drop increased for both experiments and simulations. The relationship between them seemed to be a quadratic function, and the specific expression can be seen in the following section 3 (RESULTS AND DISCUSSION). The simulations were in good agreement with the experimental values, and the maximum relative error was less than 6%. The standard k-ε model was also used to successfully predict the difference pressure with respect to the flow rate in the

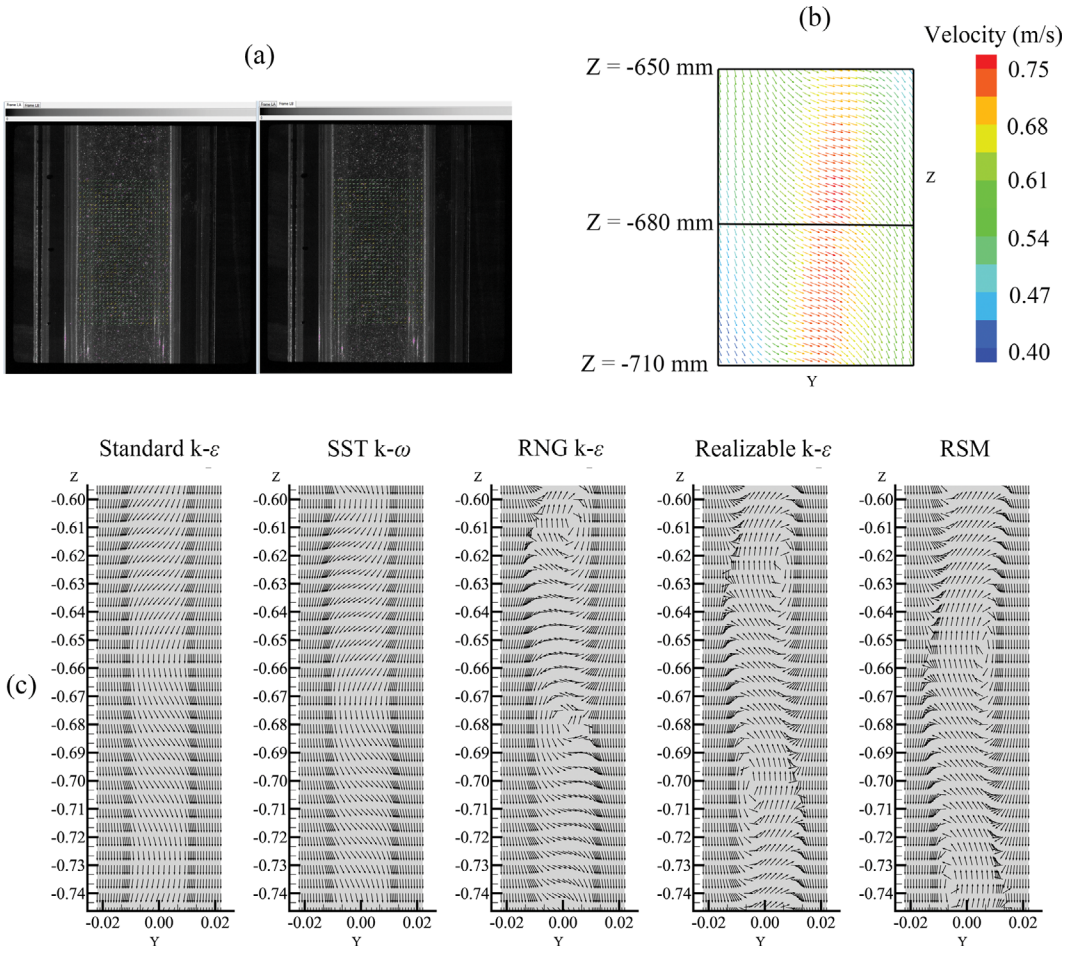


Fig. 7. (a) Image analysis results of frames A, B in Insight 4G software, (b) mean velocity vector, and (c) the velocity vector diagram of different turbulence models.

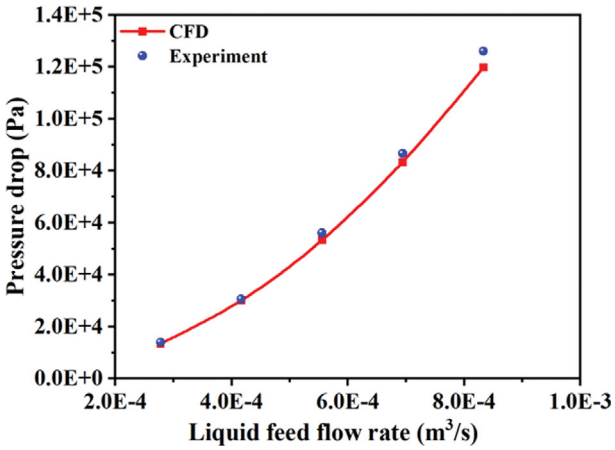


Fig. 8. Comparison of pressure drop between CFD and experiments.

axial flow pump [35]. Therefore, in this study, the standard k-ε model accurately predicted the flow field of the swirl flow bubble generator, and the model will be used in subsequent simulations.

2. Flow Field Analysis

Fig. 9 shows the streamlines of the swirl flow bubble generator with a liquid flow rate of 5.56E-4 m^3/s, an open hole number of 12, and an open hole scheme S-1_12. When the liquid entered the vortex chamber from multiple oblique holes, it generated a swirl flow in the vortex chamber and straight pipe section. The liquid spirally descended from the vortex chamber to the straight pipe section. However, its vortex flow field is weaker than traditional hydrocyclones [46] based on the PIV measurement results and turbulence model validation.

Fig. 10 shows the pressure, axial velocity, radial velocity, and tangential velocity distribution at X=0. Due to the large ratio between height and diameter of the swirl flow bubble generator, the vortex chamber region (Z=−0.23 m-0 m) was magnified to illustrate the flow pattern. In the vortex chamber, the pressure near the wall has a higher value of ~2,000 Pa than in other zones, and the low or negative pressure was concentrated in the zone of more than 60% space of the vortex chamber. In the straight pipe section part, the pressure was close to the gauge pressure of 0. The axial velocity was very complex without flow regular in the vortex chamber, which was different from the hydrocyclone axial flow profiles [46], namely, without significant quasi-free and quasi-forced vortices along the radial direction, especially in the upstream zone. The axial velocity was close to 0.10 m/s near the central region down-

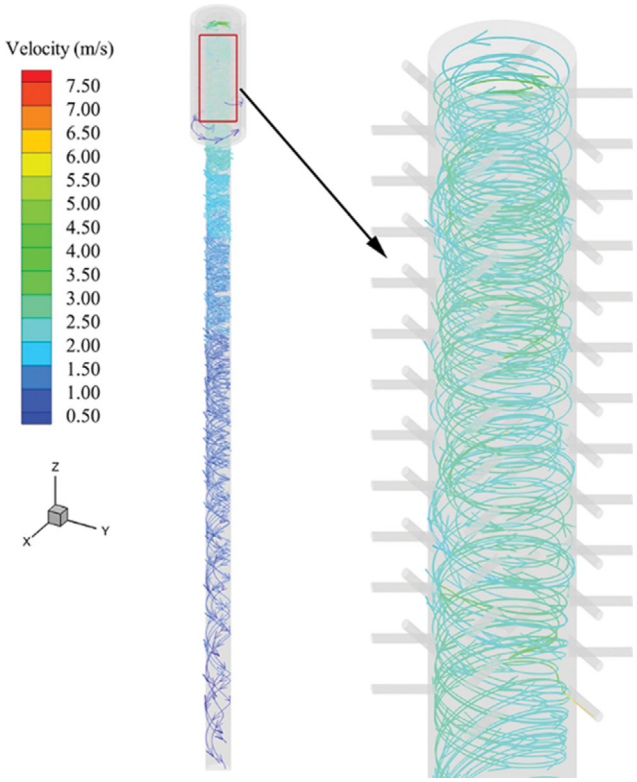


Fig. 9. Streamlines in the swirl flow bubble generator with a liquid flow rate of 5.56E-4 m^3/s, an open hole number of 12, and an open hole scheme S-1_12.

stream of the vortex chamber. With the increase in flow distance, the axial velocity was close to a constant of ~0.35 m/s. Unlike the hydrocyclone, the radial velocity could be compared with the axial velocity because of the 60° horizontal angle of the holes and the large diameter ratio of approximately 15 between the vortex chamber and hole. The positive and negative radial velocities appeared alternately along the flow direction due to the spiral flow. The tangential velocity had the largest value among the three velocity components, and the values were almost the same in the vortex chamber. The reason may be the uniform open holes along the height of the vortex chamber. Along the radial direction 0<r/R<1, the tangential velocity increased first and then decreased. The maximum tangential velocity of ~2.7 m/s was close to the wall. The tangential velocity gradually reduced in the straight pipe section due to the flow resistance.

To describe the flow field of the bubble generator further quantitatively, the velocities and turbulence characteristics in the radial direction were extracted, as shown in Fig. 11. The distribution of the mean axial velocity, radial velocity, tangential velocity, and resultant velocity in the radial position at Z=−120 mm and Z=−1,000 mm is illustrated in Fig. 11(a), (b). They show that the tangential velocity and resultant velocity were approximately symmetrical. The tangential velocity was an "M" shape. At the Z=−120 mm position in the vortex chamber, the tangential velocity from center to 0.75R increased from 0 to 2.7 m/s and then decreased because of walls. The tangential and resultant velocities were almost the same, indicating that the tangential velocity was the primary velocity component in the vortex chamber. Due to the turbulence energy consumption of fluid flow from the vortex chamber to the straight pipe section, the maximum tangential velocity dropped from 2.7 m/s to 0.65 m/s. The tangential velocity was always positive, indicating that the fluid rotated in the same direction at the vortex chamber and straight pipe section. According to the streamlines of fluid shown in Fig. 9, the rotation direction was counterclockwise. At Z=−120 mm, the axial velocity and radial velocity had equivalent values, and the conclusion was the same as Fig. 10. In the straight pipe section, the axial velocity was negative, and the radial velocity was close to 0 at Z=−1,000 mm. The axial velocity was comparable with the tangential velocity because of weak swirl flow and

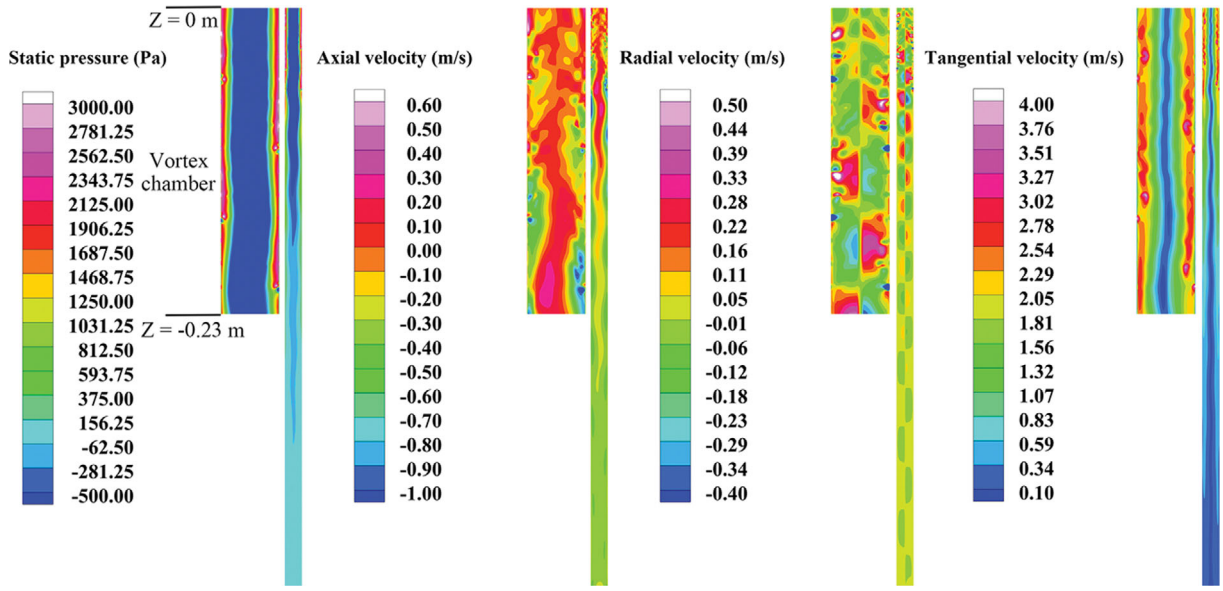


Fig. 10. The pressure, axial velocity, radial velocity, and tangential velocity distribution at X=0.

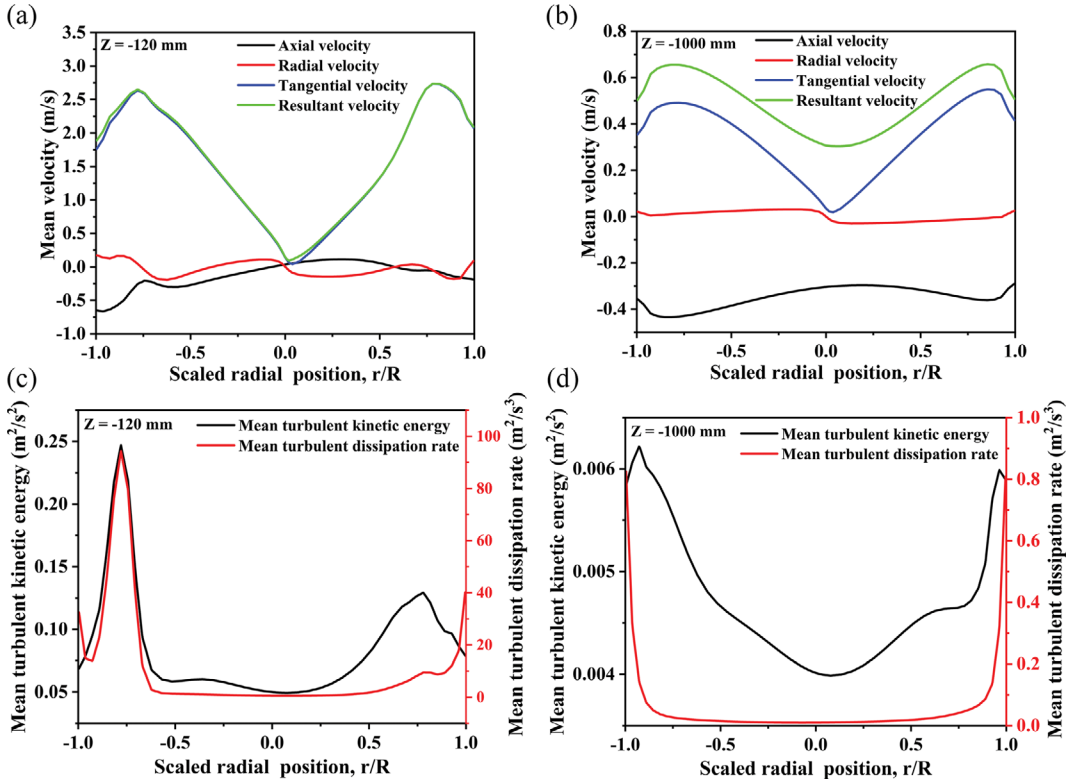


Fig. 11. Local information of flow field: (a) Z=−120 mm for mean velocity components, (b) Z=−1,000 mm for mean velocity components, (c) Z=−120 mm for mean turbulent kinetic energy and dissipation rate, and (d) Z=−1,000 mm for mean turbulent kinetic energy and dissipation rate.

gravity.

Fig. 11(c), (d) shows the mean turbulent kinetic energy and turbulent dissipation rate in the radial position at Z=−120 mm and Z=−1,000 mm. At Z=−120 mm near the liquid inlet, the maximum values of turbulent kinetic energy and turbulent dissipation rate were 0.25 m^2/s^2 and 90 m^2/s^3 because of greater hole velocity near the liquid inlet. The turbulent dissipation rate curve was flat with small values of approximately 0 in the range of −0.5R to 0.5R, indicating that the energy dissipation was mainly concentrated near the wall. At Z=−1,000 mm, due to the flow resistance, the order of magnitude for the turbulent kinetic energy and turbulent dissipation rate became 10^{-3} and 10^{-1}, respectively. There were also maximum values near the wall.

3. Open Hole Number

The characteristic of the bubble generator is that it can adapt to the change in the liquid feed flow rate. When the feed flow rate is low, the turbulence intensity in the vortex chamber becomes weaker. Plugging holes is usually used to increase the turbulent intensity of the vortex chamber. The plugging holes method refers to reducing the open hole number and increasing the flow velocity in the open holes. The greater the hole velocity, the stronger the turbulence in the vortex chamber. It is noted that the gas or bubble density is significantly less than the liquid density. Therefore, the liquid flow can reflect the actual operating status because it directly affects the entire equipment's turbulent intensity and energy consumption.

In the actual adjustment process, the turbulence intensity can be determined indirectly through the pressure drop of the equipment. However, this adjustment method needs further study to facilitate actual operation. Therefore, finding the relationship among the pressure drop, liquid feed flow rate, and open hole number is necessary to guide the operation and run.

Through the validation and selection of the turbulence model in Section 1 (RESULTS AND DISCUSSION), the relationship among the pressure drop, liquid feed flow rate, and open hole number was obtained by simulations. According to chemical engineering principles, under turbulent flow conditions, the flow pressure drop ΔP (Pa) in the pipeline is proportional to the square of the mean velocity, namely, the square of the volume flow rate Q_{lf} (m^3/s). The relationship can be described as follows:

$$\Delta P = kQ_{lf}^2 \tag{29}$$

Fig. 12(a), (b) shows the relationship between pressure drop ΔP and the feed flow rate Q_{lf}. The ΔP was proportional to Q_{lf}^2 at the same open hole number, and Eq. (29) held for both even and odd open hole numbers. With the increase in the open hole number, the proportional coefficient k decreased, and the variation tendency was plotted in Fig. 12(c). The proportional coefficient k increased approximately exponentially with the decrease of the open hole number N, indicating that the ΔP was more sensitive to the variation of Q_{lf} when the open hole number was small. Therefore, the plugging hole adjustment method was limited when the Q_{lf} was low. The relationship between k and N was plotted in the double logarithmic coordinate and linear fitting regression, as shown in Fig. 12(d). Finally, the relationship among ΔP, N, and Q_{lf} was ob-

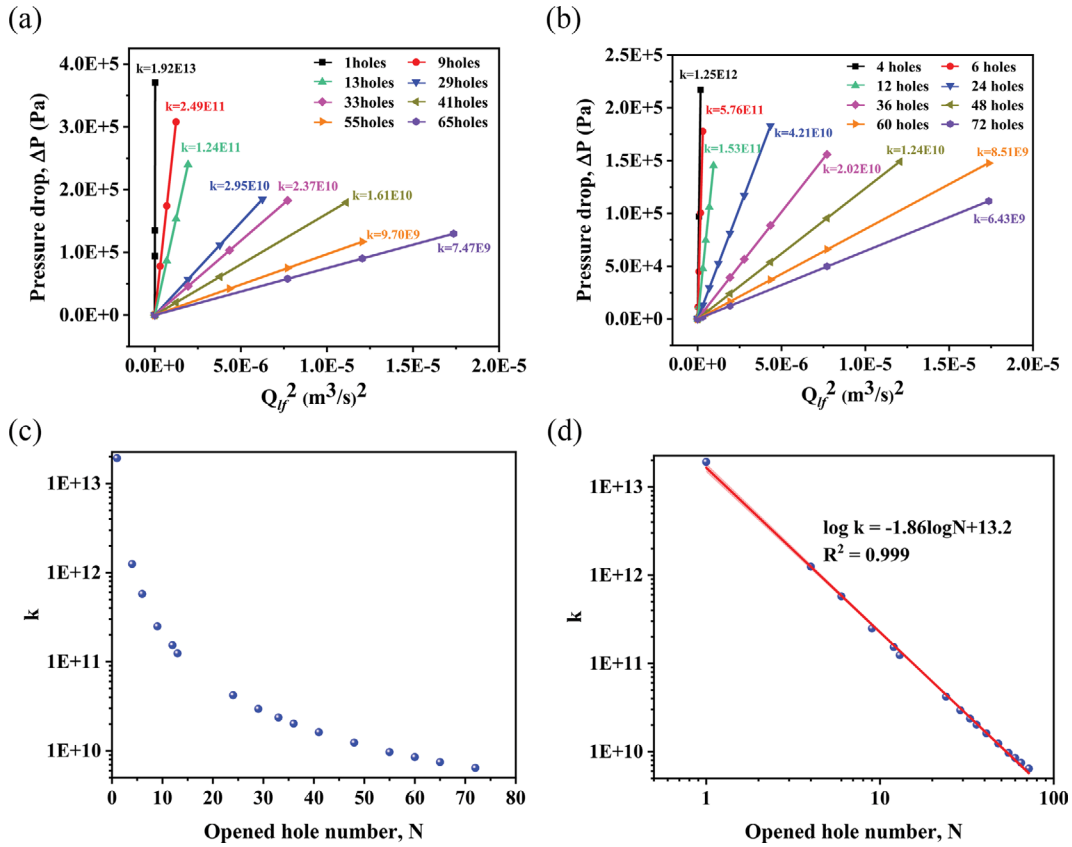


Fig. 12. The relationship among pressure drop, feed flow rate, and open hole number from simulations: (a) odd open hole number, (b) even open hole number, (c) scatter diagram, and (d) log-linear fitting.

tained, expressed by Eq. (30). The parameters a and b, respectively, were 1.58E13 and 1.86. Notably, ΔP was negatively correlated with N and positively correlated with Q_{lf}. The smaller the open hole number, the greater the pressure drop at a constant feed flow rate. Eq. (30) correctly represents the relationship among the pressure drop, the open hole number, and the feed flow rate. It provides great convenience for the actual operation.

$$\Delta P = \frac{aQ_{lf}^2}{N^b} = \frac{a\pi^2 D_{il}^4 u_0^2}{16N^b} \tag{30}$$

where ΔP is the pressure drop of the swirl flow bubble generator. Q_{lf} is the liquid feed flow rate. N refers to the number of open holes. D_{il} denotes the liquid inlet diameter.

Eq. (30) reflects the relationship among pressure drop of the swirl flow bubble generator, open hole number, and feed flow rate from a macroscopic and global perspective. However, as shown in Fig. 12(a), the same pressure drop corresponds to different feed flow rates and open hole number. Fig. 13 illustrates their influences on the tangential velocity, turbulent dissipation rate, and Q criterion of the vortex chamber at a pressure drop of approximately 55 kPa. Five cases of open hole number and feed flow rates were selected to compare: (A) N=12, Q_{lf}=5.56E-4 m^3/s; (B) N=29, Q_{lf}=1.31E-3 m^3/s; (C) N=36, Q_{lf}=1.58E-3 m^3/s; (D) N=55, Q_{lf}=2.28E-3 m^3/s; (E) N=72, Q_{lf}=2.78E-3 m^3/s.

When the pressure drop was approximately the same, the larger the feed flow rate, the greater the open hole number. The mean tangential velocity increased with the increase in feed flow rate. From A to E, the maximum tangential velocity increased by approximately 35%. Furthermore, a region width with a low velocity of less than 1.0 m/s in the vortex chamber decreased by 44%. Due to the increase in open hole number, the tangential velocity became more uniform in the vortex chamber, which can also be reflected in the mean turbulent dissipation rate, as shown in Fig. 13(b). The turbulent dissipation rate was mainly distributed in the wall region, and from A to E, the maximum turbulent dissipation rate was all almost close to 50 m^2/s^3 because of the similar hole velocity. The central region dissipation rate increased from A to E. High turbulence intensity is conducive to the generation of tiny bubbles [47]. Furthermore, Fig. 13(c) displays the Q criterion (Q>0) in the vortex chamber. The vorticity was mainly concentrated in the central region. Near the wall, the vorticity was close to null, and the strain rate dominated. From A to E, the maximum vorticity gradually transferred to the center, and the maximum value increased by four times. It means that at a higher feed flow rate and more open hole number, the energy in the vortex chamber is adequate, and the gas phase is easier to break into tiny bubbles.

4. Open Hole Scheme

The relationship among the pressure drop, feed flow rate, and open hole number was established in Section 3 (RESULTS AND DISCUSSION). In this section, the pressure drop and the mean

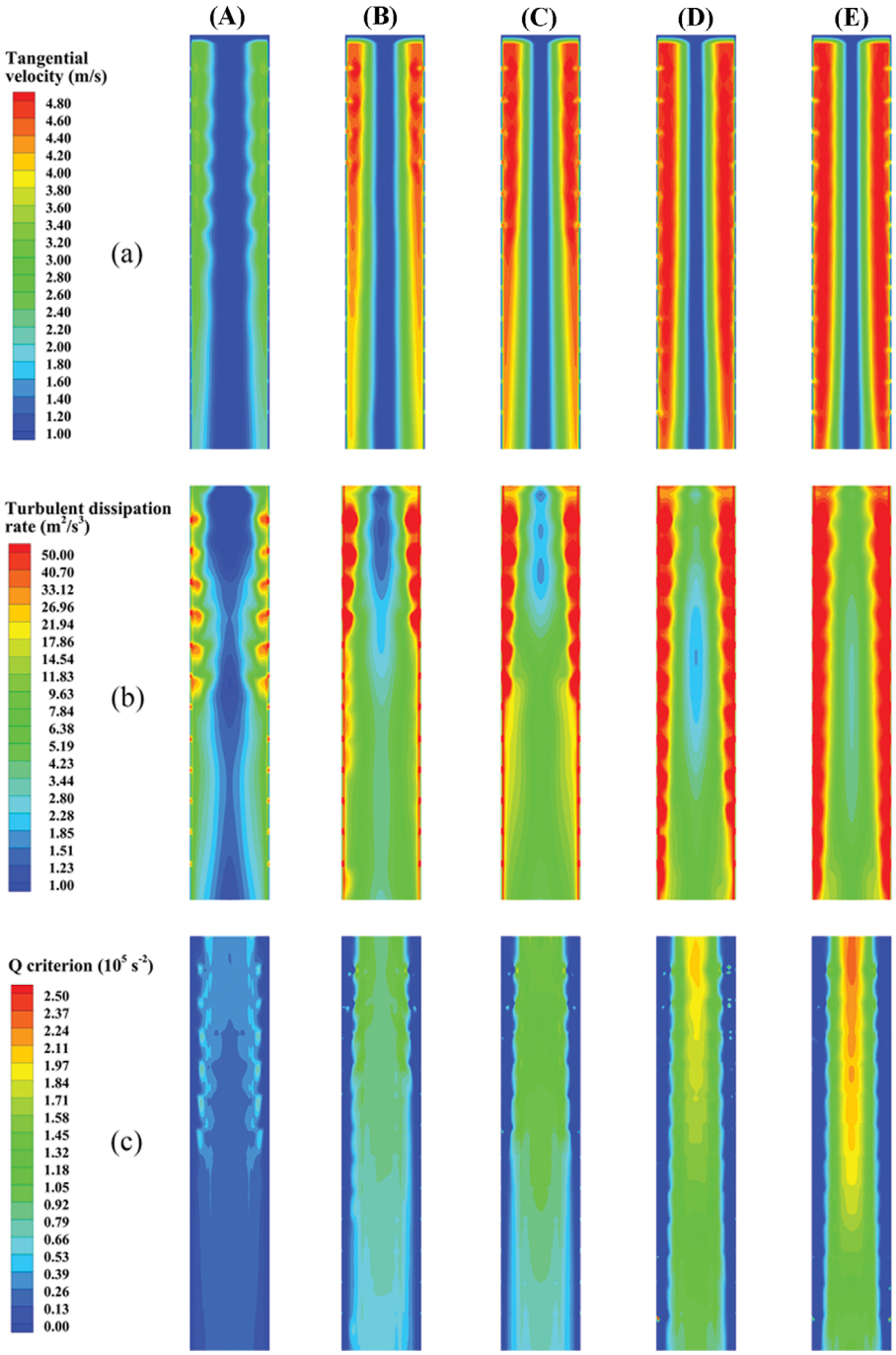


Fig. 13. Effect of various feed flow rates and open hole numbers on the flow field in the vortex chamber at the same pressure drop of 55 kPa (X=0): (a) tangential velocity, (b) turbulent dissipation rate, and (c) Q criterion. ((A) N=12, Q_{lf}=5.56E-4 m^3/s; (B) N=29, Q_{lf}=1.31E-3 m^3/s; (C) N=36, Q_{lf}=1.58E-3 m^3/s; (D) N=55, Q_{lf}=2.28E-3 m^3/s; (E) N=72, Q_{lf}=2.78E-3 m^3/s).

turbulent dissipation rate in the vortex chamber and the straight pipe section were selected to express the differences in the open hole schemes. The pressure drop represents the energy consumption. The dissipation rate is relative to the bubble diameter. The maximum stable bubble diameter can be estimated by Eq. (31) [47].

$$D_{Max} = A\varepsilon^{-2/5}\sigma^{3/5}\rho^{-3/5} \quad (31)$$

where D_{Max} is the maximum stable bubble diameter. A represents a proportional constant. ε is the turbulent dissipation rate. σ denotes the surface tension. ρ refers to the density of the liquid phase.

Fig. 14(a) shows that the variation in pressure drop caused by different open hole schemes can be ignored. The abscissa denotes the open hole schemes as displayed in Fig. 5. When the feed flow rate was 5.56E-4 m^3/s and the open hole number was set as 12, the pressure drop was approximately 55 kPa in all cases. So Eq. (30) can apply to all open schemes. The pressure drop did not effec-

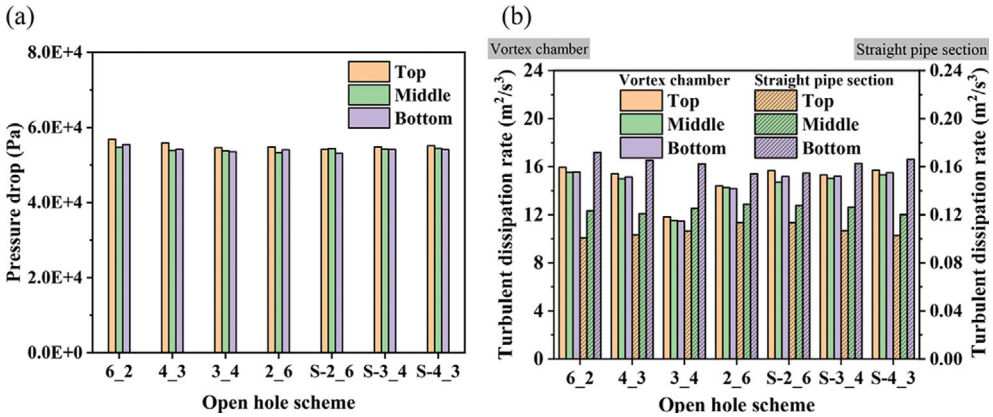


Fig. 14. Effect of different open hole schemes: (a) pressure drop, and (b) turbulent dissipation rate.

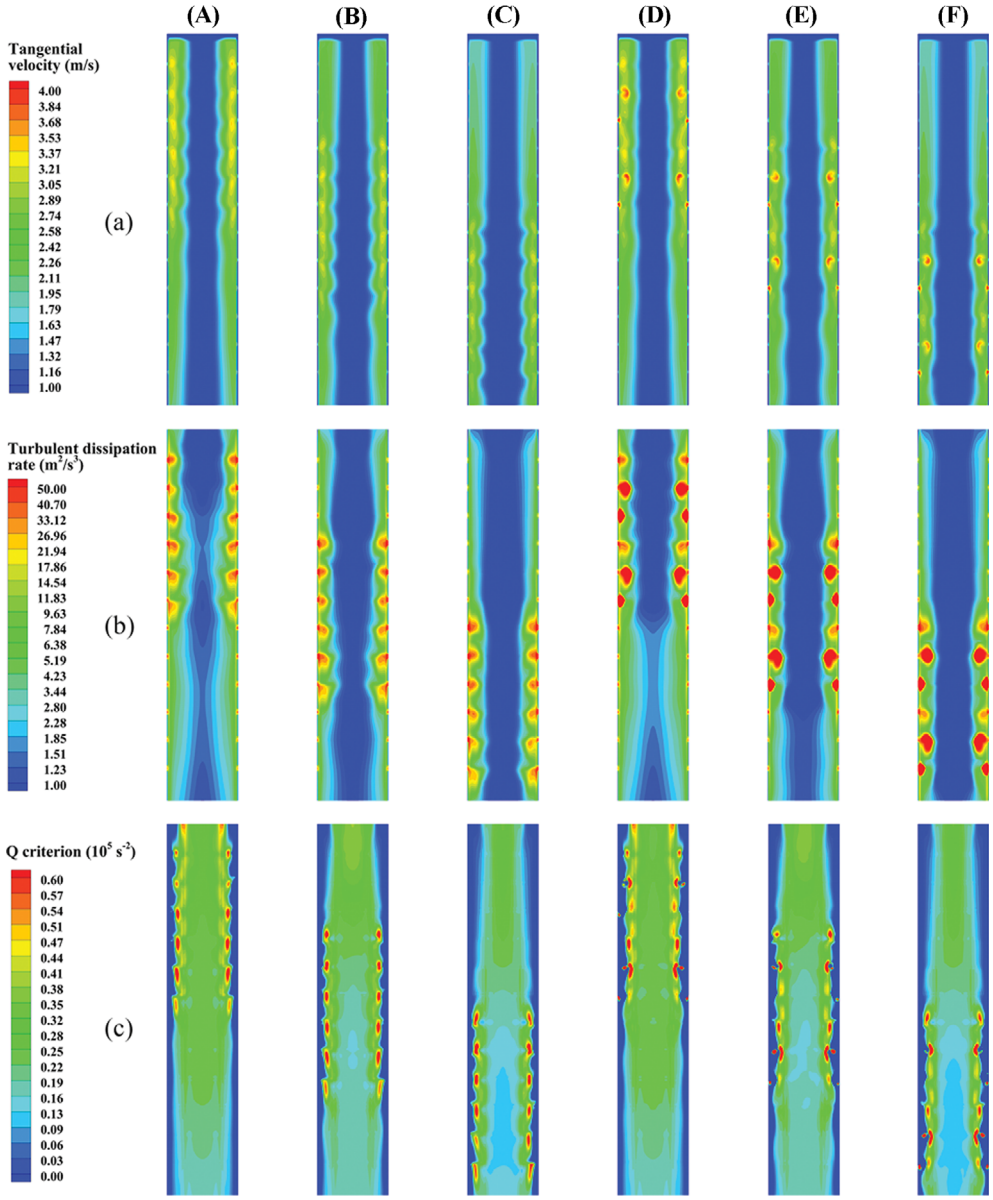


Fig. 15. Effect of open hole schemes on the flow field in the vortex chamber (X=0): (a) tangential velocity, (b) turbulent dissipation rate, and (c) Q criterion. ((A) above-2_6; (B) middle-2_6; (C) bottom-2_6; (D) spiral-above-2_6; (E) spiral-middle-2_6; (F) spiral-bottom-2_6).

tively illustrate the difference in the open hole schemes.

As shown in Fig. 14(b), the mean turbulent dissipation rate in the vortex chamber and the straight pipe section was different among the open hole schemes. In the vortex chamber, when the open hole schemes were 3_4, the turbulent dissipation rate of the vortex chamber had a minimum value of 12 m^2/s^3. When the spiral open hole schemes were used, the turbulent dissipation rate increased to 14-16 m^2/s^3, indicating that the spiral open hole schemes helped increase the turbulent dissipation rate of the vortex chamber and reduced the maximum stable bubble diameter. In the straight pipe section, the turbulent dissipation rate was two orders of magnitude lower than that of the vortex chamber. Compared to the top and middle open hole schemes, the turbulent dissipation rate in the straight pipe section could be enhanced by 41.2% and 29.4% for the bottom open hole scheme, respectively. This is because the bottom open hole scheme is located at the junction of the vortex chamber and the straight pipe section, and it increases the turbulence intensity at the inlet of the straight pipe section and the overall turbulent dissipation rate of the straight pipe section. Based on the above analysis of the open hole schemes, the spiral-bottom open hole schemes can be selected to enhance the turbulent dissipation of the vortex chamber and the straight pipe section.

The influences of different open hole schemes on the flow field in the vortex chamber are illustrated in Fig. 15. Here, spiral (S-2_6) and non-spiral (2_6) open hole schemes are compared. A, B, C, D, E, and F denote above-2_6, middle-2_6, bottom-2_6, spiral-above-2_6, spiral-middle-2_6, and spiral-bottom-2_6 open hole schemes, respectively. The tangential velocity has a similar velocity distribution pattern. The maximum tangential velocity exists at the location of open holes. At these positions, the tangential velocity is a uniform distribution for the non-spiral open hole schemes compared with that of spiral open hole schemes. However, the maximum tangential velocity of ~3.5 m/s in the spiral open hole schemes is greater than that of the non-spiral open hole schemes. When the open hole number is 12, the velocities in the holes are approximately equal to 6.5 m/s. In the non-spiral scheme, the tangential velocity is small because the fluid from the upper and lower holes always comes into the same radial position in the vortex chamber. The spiral schemes can ensure that fluid enters the vortex chamber in the entire circumference of the vortex chamber. This can make tangential velocity higher. Meanwhile, the variation in the turbulent dissipation rate and Q criterion between spiral and non-spiral schemes is similar to that of the tangential velocity. The maximum turbulent dissipation rate of the spiral open hole schemes near the hole outlet was 50 m^2/s^3, which was 40% higher than that of the non-spiral open hole schemes. The maximum Q criterion value was also distributed near the hole outlet, and the spiral open hole schemes had higher values than non-spiral schemes. The analysis indicates that the spiral open hole scheme is beneficial to the generation of bubbles.

CONCLUSIONS

We performed PIV tests and CFD simulations of a unique swirl flow bubble generator. Results with different turbulence models were compared with PIV data at the straight pipe section. The results show that the axial velocity distribution predicted by the standard k-ε model agreed well with PIV data compared to other turbulence models. The velocity vectors calculated by the standard k-ε model were more in accordance with the actual flow pattern. The maximum pressure drop difference between CFD simulations and experiments was less than 6%. The relationship among the pressure drop, open hole number, and feed flow rate was obtained by CFD simulations. The pressure drop was proportional to the feed flow rate or inlet velocity square and inversely proportional to the power of 1.86 open hole number. The expression was suitable for both odd and even open hole numbers. The pressure drop in different open hole schemes at the same open hole number of 12 was approximately 55 kPa, which indicated that the open hole scheme was not a sensitivity parameter for the pressure drop. The established expression could be used without considering the difference in the open hole scheme at the same open hole number. However, the effect of the open hole scheme on the turbulent dissipation rate was significant. The vortex chamber had a minimum turbulent dissipation rate value of ~12 m^2/s^3 for the open hole scheme 3_4. When the spiral-open hole schemes were adopted, the turbulent dissipation could increase to 14-16 m^2/s^3. Meanwhile, compared to the top and middle open hole schemes, the turbulent dissipation rate in the straight pipe section could be enhanced by 41.2% and 29.4% for the bottom open hole scheme, respectively. Therefore, the spiral-bottom open hole schemes are suggested to ensure high turbulent dissipation rates in both the vortex chamber and straight pipe section. This work can provide an adjustment guideline for the swirl flow bubble generator from the theoretical level and fill the gap in this respect.

It should be pointed out that the numerical simulation was based on single-phase flow without considering the effect of the gas phase or bubble in this work. The bubble generation performance was qualitatively judged according to the turbulent dissipation rate in the vortex chamber and straight pipe section. In further work, we will consider the multiphase flow study using the computational fluid dynamics-population balance model (CFD-PBM) method to explore the performance of bubble generation based on the current work.

ACKNOWLEDGEMENTS

The authors gratefully acknowledge the support of the calculation resource provided by professor Jianguo Yu.

CREDIT AUTHOR CONTRIBUTIONS

Yuxue Wu: Methodology, Software, Writing-original draft. Hang Chen: Data curation, Formal analysis. Xingfu Song: Validation, Supervision, Writing-review & editing.

NOMENCLATURE

Abbreviations

3D : three-dimensional
CAD : computer aided design
CCD : charge coupled device

CFD : computational fluid dynamics
CWT : clean water technology
ICEM : Integrated computer engineering and manufacturing
PBM : population balance model
PISO : pressure-implicit with splitting of operators
PIV : particle image velocimetry
PRESTO : pressure staggering option
QUICK : quadratic upstream interpolation for convective kinematics
RANS : Reynolds averaged Navier-Stokes
RNG : renormalization group
RSM : Reynolds stress model
SCDM : SpaceClaim direct modeler
SST : shear stress transport

Notations

A : constant of proportional [-]
a, b : model parameters [-]
d : hole diameter [m]
D_{ci} : internal diameter of cavity [m]
D_{co} : outer diameter of cavity [m]
D_{ia} : inlet diameter for gas phase [m]
D_{il} : inlet diameter for liquid phase [m]
D_{Max} : maximum stable bubble diameter [m]
D_o : diameter of vortex chamber and straight pipe section [m]
$D_{T_{ij}}$: turbulent diffusion term in Reynolds Stress Model [kg/m/s^3]
E_{ij} : time-averaged strain rate [1/s]
F_{ij} : production of system rotation term in Reynolds Stress Model [kg/m/s^3]
G_k : generation term of turbulent kinetic energy resulting from the mean velocity gradient [kg/m/s^3]
G_ω : generation term of specific dissipation rate [kg/m^3/s^2]
H : total height [m]
h : height of the vortex chamber [m]
k : proportional coefficient (–) or turbulent kinetic energy [m^2/s^2]
N : open hole number [-]
p : pressure [Pa]
P_{ij} : stress production term in Reynolds Stress Model [kg/m/s^3]
Q : Q criterion [1/s^2]
Q_{lf} : liquid feed flow rate [m^3/s]
r : radial position [m]
R : radius [m]
S : spiral open hole scheme [-]
t : time [s]
u : velocity [m/s]
u_0 : liquid inlet velocity [m/s]
x : space coordinate [m]
Y_k : dissipation of turbulent kinetic energy due to turbulence [kg/m/s^3]
Y_ω : dissipation of specific dissipation rate due to turbulence [kg/m^3/s^2]
Z : axial position [m]
ΔP : pressure drop [Pa]

Greek Letters

α : inclination angle of the holes [°]
ε : turbulent dissipation rate [m^2/s^3]
ε_{ij} : dissipation term in Reynolds Stress Model [kg/m/s^3]
θ : angle of hole arrangement [°]
μ : viscosity [Pa·s]
μ_t : turbulent viscosity [Pa·s]
ρ : density [kg/m^3]
σ : surface tension [N/m]
σ_k : Prandtl number for turbulent kinetic energy k
σ_ε : Prandtl number for turbulent dissipation rate ε
ω : specific dissipation rate [1/s]
ω_k : angular velocity [1/s]
$\tilde{\Omega}_{ij}$: mean rate-of-rotation tensor [1/s]
ϕ_{ij} : pressure strain term in Reynolds Stress Model [kg/m/s^3]

REFERENCES

1. H. X. Xu, J. T. Liu, L. H. Gao, Y. T. Wang, X. W. Deng and X. B. Li, *Sep. Sci. Technol.*, **49**, 1170 (2014).
2. X. L. Cai, J. Q. Chen, M. L. Liu, Y. P. Ji and S. An, *Sep. Purif. Technol.*, **176**, 134 (2017).
3. J. Saththasivam, K. Loganathan and S. Sarp, *Chemosphere*, **144**, 671 (2016).
4. Q. Huang and X. Y. Long, *Energies*, **13**, 927 (2020).
5. Y. R. Feng, H. F. Mu, X. Liu, Z. L. Huang, H. M. Zhang, J. D. Wang and Y. R. Yang, *Ind. Eng. Chem. Res.*, **59**, 8447 (2020).
6. Y. F. Wang, Z. C. Pan, J. Fen and Q. W. Qing, *Miner. Eng.*, **145**, 106066 (2020).
7. B. Q. Xie, C. J. Zhou, J. X. Chen, X. T. Huang and J. S. Zhang, *Chem. Eng. Sci.*, **247**, 117105 (2022).
8. H. S. Alam, P. Sutikno, T. A. Fauzi Soelaiman and A. T. Sugiarto, *Eng. Appl. Comp. Fluid Mech.*, **16**, 677 (2022).
9. K. Terasaka, A. Hirabayashi, T. Nishino, S. Fujioka and D. Kobayashi, *Chem. Eng. Sci.*, **66**, 3172 (2011).
10. Y.-B. Kim, H.-S. Lee, L. Francis and Y.-D. Kim, *J. Membr. Sci.*, **588**, 117197 (2019).
11. X. Y. Wang, Y. Shuai, X. R. Zhou, Z. L. Huang, Y. Yang, J. Y. Sun, H. M. Zhang, J. D. Wang and Y. R. Yang, *Chem. Eng. Process.*, **154**, 108022 (2020).
12. M. Wu, S. Y. Yuan, H. Y. Song and X. B. Li, *Chem. Eng. Process.*, **170**, 108697 (2022).
13. I. Levitsky, D. Tavor and V. Gitis, *Chem. Eng. Technol.*, **39**, 1537 (2016).
14. X. Xu, X. L. Ge, Y. D. Qian, B. H. Zhang, H. L. Wang and Q. Yang, *Chem. Eng. Res. Des.*, **138**, 13 (2018).
15. D. I. Mawarni, W. E. Juwana, K. A. Yuana, W. Budhijanto, Deendarlianto and Indarto, *J. Water Process Eng.*, **48**, 102846 (2022).
16. Y. L. Chang, L. Xu, J. P. Li, X. Jiang, Y. Huang, W. J. Lv and H. L. Wang, *Ind. Eng. Chem. Res.*, **60**, 1423 (2021).
17. M. Colic, W. Morse and J. D. Miller, *Int. J. Environ. Pollut.*, **30**, 296 (2007).
18. A. R. Al-Obaidi, *Exp. Tech.*, **44**, 329 (2020).
19. A. R. Al-Obaidi and R. Mishra, *Arabian J. Sci. Eng.*, **45**, 5657 (2020).
20. A. R. Al-Obaidi, *Heliyon*, **5**, e01910 (2019).
21. A. R. Al-Obaidi and H. Towsyfyan, *J. Appl. Fluid Mech.*, **12**, 2057 (2019).
22. A. R. Al-Obaidi, *Arch. Acoust.*, **45**, 541 (2020).

23. A. R. Al-Obaidi, *Int. J. Fluid Mech. Res.*, **47**, 501 (2020).
24. A. R. Al-Obaidi, *Arch. Acoust.*, **44**, 59 (2019).
25. X. H. Li, W. B. Su, Y. Liu, X. K. Yan, L. J. Wang and H. J. Zhang, *Asia-Pac. J. Chem. Eng.*, **16**, e2611 (2020).
26. S. L. Yan, Y. Zhang, C. Peng, X. Y. Yang, Y. Huang, Z. S. Bai and X. Xu, *Chin. J. Chem. Eng.*, **45**, 229 (2022).
27. S. L. Yan, Y. Zhang, X. Y. Yang, Y. Huang, Z. S. Bai and X. Xu, *Ind. Eng. Chem. Res.*, **60**, 6006 (2021).
28. X. K. Yan, Y. P. Yao, S. Q. Meng, S. Y. Zhao, L. J. Wang, H. J. Zhang and Y. J. Cao, *Chem. Eng. Res. Des.*, **174**, 1 (2021).
29. A. R. Al-Obaidi, *Int. J. Nonlinear Sci. Numer. Simul.*, **20**, 487 (2019).
30. A. R. Al-Obaidi, *J. Mech. Eng. Sci.*, **14**, 6570 (2020).
31. A. R. Al-Obaidi, *Heat Transfer*, **49**, 2000 (2020).
32. A. R. Al-Obaidi, *J. Appl. Fluid Mech.*, **12**, 445 (2019).
33. A. R. Al-Obaidi, *J. Phys. Conf. Ser.*, **1279**, 012069 (2019).
34. A. R. Al-Obaidi, *Int. J. Model. Simul. Sci. Comput.*, **12**, 2150045 (2021).
35. A. R. Al-Obaidi and A. A. Mohammed, *J. Eng. Sci. Technol. Rev.*, **12**, 70 (2019).
36. A. R. Al-Obaidi, *Iran. J. Sci. Technol. Trans. Mech. Eng.*, **45**, 441 (2021).
37. X. Y. Wang, Y. Shuai, H. M. Zhang, J. Y. Sun, Y. Yang, Z. L. Huang, B. B. Jiang, Z. W. Liao, J. D. Wang and Y. R. Yang, *Chem. Eng. J.*, **403**, 126397 (2021).
38. B. E. Launder and D. B. Spalding, *Lectures in mathematical models of turbulence*, Academic Press, London, England (1972).
39. V. Yakhot and S. A. Orszag, *J. Sci. Comput.*, **1**, 3 (1986).
40. T.-H. Shih, W. W. Liou, A. Shabbir, Z. Yang and J. Zhu, *Comput. Fluids*, **24**, 227 (1995).
41. F. R. Menter, *AIAA J.*, **32**, 1598 (1994).
42. B. E. Launder, G. J. Reece and W. Rodi, *J. Fluid Mech.*, **68**, 537 (1975).
43. M. M. Gibson and B. E. Launder, *J. Fluid Mech.*, **86**, 491 (1978).
44. B. E. Launder, *Int. J. Heat Fluid Flow*, **10**, 282 (1989).
45. P. Yan, H. B. Jin, G. X. He, X. Y. Guo, L. Ma, S. H. Yang and R. Y. Zhang, *Chem. Eng. Res. Des.*, **154**, 47 (2020).
46. J. X. Ye, Y. X. Xu, X. F. Song and J. G. Yu, *Chem. Eng. Res. Des.*, **144**, 135 (2019).
47. J. O. Hinze, *AIChE J.*, **1**, 289 (1955).